ARTICLE

The Electronic Structure of a β-Diketiminate Manganese Hydride Dimer

Changjin Oh,[a,b] Joëlle Siewe,[b,c] Thao T. Nguyen,[d] Airi Kawamura,[e] Marco Flores,[d] Thomas L. Groy,[d] John S. Anderson,[e] Ryan J. Trovitch*[d] and Mu-Hyun Baik*[a,b]

The electronic structure of a dimeric manganese hydride catalyst supported by β-diketiminate ligands, $[(^{2,6\text{-}iPr2Ph}BDI)Mn(\mu\text{-}H)]_2$, was investigated with density functional theory. A triple bond between the manganese centers was anticipated from simple electron-counting rules; however, calculations revealed Mn–Mn Mayer bond orders of 0.21 and 0.27 for the ferromagnetically-coupled and antiferromagnetically-coupled extremes, respectively. In accordance with experimentally determined Heisenberg exchange coupling constants of -15 ± 0.1 cm^{-1} (SQUID) and -10.2 ± 0.7 cm^{-1} (EPR), the calculated J_o value of -10.9 cm^{-1} confirmed that the ground state involves antiferromagnetic coupling between high spin Mn(II)-d^5 centers. The effect of steric bulk on the bond order was interrogated via a model study with the least sterically-demanding version of the β-diketiminate ligand and was found to be negligible. Mixing between metal- and β-diketiminate-based orbitals was found to be responsible for the absence of a metal–metal multiple bond. The bridging hydrides give rise to a relatively close positioning of the metal centers, while bridging atoms possessing 2p-orbitals result in longer Mn-Mn distances and more stable dimers. The sythesis and characterization of the bridging hydroxide variant, $[(^{2,6\text{-}iPr2Ph}BDI)Mn(\mu\text{-}OH)]_2$, provides experimental support for these assessments.

Introduction

Transition metal complexes featuring coordinatively- and electronically-unsaturated ligand environments exhibit rich reactivity and have been extensively studied.[1] It is widely acknowledged that bulky ligands can stabilize low-coordinate and electron-deficient complexes by preventing aggregation.[2] One ubiquitous class of bulky ligands that support electron-deficient metal centers is based on the β-diketiminate ligand, commonly abbreviated as BDI or nacnac. Practical advantages such as facile synthesis and easy modification[3] enable systematic studies on β-diketiminate ligands.[4,5] For instance, Mindiola reported catalytic carboamination with a titanium complex supported by a β-diketiminate ligand.[6] Holland described a Fe(II) fluoride β-diketiminate complex that catalyzes the hydrodefluorination of fluorocarbons.[7] Despite extensive investigations on transition metal complexes supported by β-diketiminate ligands, (BDI)Mn complexes have only recently been found to exhibit catalytic activity. Notably, the bridging hydride dimer $[(^{2,6\text{-}iPr2Ph}BDI)Mn(\mu\text{-}H)]_2$ (**1**) has been structurally characterized and found to catalyze the hydrosilylation of alkenes[8] and the dihydroboration of nitriles.[9]

Intuitively, one may argue that complex **1**, which has 13 electrons per metal center formally, should feature metal–metal bonding to compensate for its low electron count, as shown in Fig. 1. The existence of a metal–metal triple bond would provide three additional electrons, allowing each Mn center to reach a 16-electron configuration. Dimeric β-diketiminate manganese complexes have been reported previously;[10–12] however, a detailed analysis of their electronic structures has not been carried out. The presence of bridging hydride ligands in **1** poses a challenge from an electronic structure perspective and deserves special attention. In this contribution, the electronic structure of **1** and related complexes featuring bridging p-block ligands are explored using a combination of computational and experimental techniques. Given that the coordinatively- and electronically-unsaturated nature of monomeric (BDI)Mn moieties render them capable of catalyzing hydrofunctionalization reactions,[8,9] the main goal of this research was to interrogate why hydride compound **1** exhibits catalytic activity.

[a.] Department of Chemistry, Korea Advanced Institute of Science and Technology (KAIST), Daejeon 34141, South Korea.
[b.] Center for Catalytic Hydrocarbon Functionalizations, Institute for Basic Science (IBS), Daejeon 34141, South Korea.
[c.] Department of Chemistry, Debye Institute for Nanomaterials Science, Utrecht University, Universiteitsweg 99, 3584 CG Utrecht, The Netherlands.
[d.] School of Molecular Sciences, Arizona State University, Tempe, AZ 85287, USA.
[e.] Department of Chemistry, The University of Chicago, Chicago, IL 60637, USA.

a)

	Electrons	Charge
Ligand		
BDI	4	−1
Hydrides	4	−1
Metal		
Mn	5	2
Total	13	0

b)

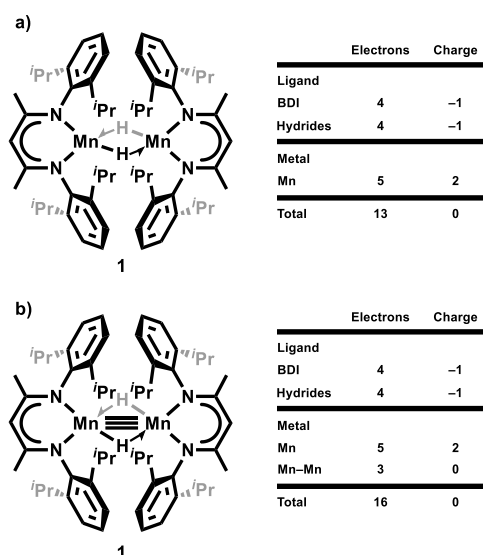|	Electrons	Charge
Ligand		
BDI	4	−1
Hydrides	4	−1
Metal		
Mn	5	2
Mn–Mn	3	0
Total	16	0

Fig. 1 Electron-count diagrams of a) **1** excluding metal–metal bonding and b) **1** including a triple bond between the manganese centres. The number of electrons per metal centre is calculated using the ionic model.[13]

Experimental

Computational details

All calculations were performed using density functional theory (DFT) as implemented in the Jaguar 9.1 suite of ab initio quantum chemistry programs.[14] The B3LYP functional[15,16] with Grimme's D3[17] dispersion correction (B3LYP-D3) was employed as the standard, together with the 6-31G** basis set for geometry optimizations. The Los Alamos LACVP basis was used to represent manganese.[18–20] In order to obtain more reliable energies, single point calculations were performed on the optimized geometries using Dunning's correlation-consistent triple-ζ cc-pVTZ(-f) basis set for main group elements and LACV3P for manganese.[21] The zero-point energy (ZPE), entropic and solvation contributions to the Gibbs energy are obtained from the same level of theory as the geometry optimizations (B3LYP-D3/6-31G**/LACVP). Energy decomposition was computed with the B3LYP-D3 functional using the Amsterdam Density Functional (ADF 2019) package.[22] The optimized geometries were confirmed to be the local minima on the potential energy surfaces by showing the absence of an imaginary frequency. The solvation calculations utilized a self-consistent reaction field (SCRF) approach on the gas phase geometry to model the solvation shell of dielectric constants ε = 2.284 for benzene and ε = 2.397 for toluene. As is the case for all continuum models, the solvation energies are subject to empirical parametrization of the atomic radii that are used to generate the solute surface.[23] We employed the standard set of optimized radii in Jaguar for H (1.150 Å), C(1.900 Å), N(1.600 Å), O(1.600 Å), F(1.682 Å) and Mn(1.480 Å).

The energy components have been computed with the following protocol. The free energy in solution phase G$_{(sol)}$ has been calculated as follows:

$$G_{(sol)} = G_{(gas)} + G_{(solv)} \tag{1}$$

$$G_{(gas)} = H_{(gas)} - TS_{(gas)} \tag{2}$$

$$H_{(gas)} = E_{(SCF)} + ZPE \tag{3}$$

$$\Delta E_{(SCF)} = \Sigma E_{(SCF)} \text{ for products} - \Sigma E_{(SCF)} \text{ for reactants} \tag{4}$$

$$\Delta G_{(sol)} = \Sigma G_{(sol)} \text{ for products} - \Sigma G_{(sol)} \text{ for reactants} \tag{5}$$

G$_{(gas)}$ is the gas phase free energy; G$_{(solv)}$ is the free energy of solvation; H$_{(gas)}$ is the gas phase enthalpy; T is the temperature (298.15 K); $S_{(gas)}$ is the gas phase entropy; E$_{(SCF)}$ is the electronic energy derived from the SCF method and ZPE is the zero-point energy.

In principle, multi-reference methods such as CASSCF are required to rigorously describe an antiferromagnetically coupled spin state of the dimer, which is impracticable for systems of this size because of computational demands. In practice, Noodleman's broken-symmetry (BS) approach,[24] which makes use of the Heisenberg spin operator formalism to obtain a reasonable electronic structure description of transition metal dimers, provides a working protocol for single reference methods such as DFT employing the unrestricted spin formalism. We carefully followed the protocol described elsewhere[25] to obtain the BS orbitals and used the unrestricted spin formalism in all calculations. Essentially, the valence bond descriptions of the molecules were used as initial guesses to generate a molecular wavefunction in terms of localized orbitals that undergo the SCF procedure.

Experimental details

All reactions were performed inside an MBraun glovebox under an atmosphere of purified nitrogen. Toluene, tetrahydrofuran, diethyl ether, and pentane were purchased from Sigma-Aldrich, purified using a Pure Process Technology solvent system, and stored in the glovebox over activated 4 Å molecular sieves and potassium before use. Celite was obtained from Oakwood Chemicals. [($^{2,6-iPr2Ph}$BDI)Mn(μ-H)]$_2$ (**1**)[8] was synthesized according to the literature procedure. Elemental analysis was performed at Robertson Microlit Laboratories Inc. (Ledgewood, NJ). Ambient temperature solid-state magnetic susceptibility was recorded using a Johnson Matthey magnetic susceptibility balance calibrated with HgCo(SCN)$_4$ and K$_3$Fe(CN)$_6$. Infrared spectra were collected on a Bruker VERTEX 70 spectrophotometer with an MCT detector.

SQUID Magnetometry

Bulk magnetometry measurements were carried out on a Quantum Design MPMS 3 equipped with a superconducting quantum interference device (SQUID) detector. Corrections were made for the diamagnetic contributions from the polycarbonate capsules and eicosane wax used to secure the sample by measuring temperature vs. moment in triplicate for each to determine a moment per gram correction. Diamagnetic corrections for the complex were made using Pascal's constants.[26]

Fitting of the χT vs. T data to the Hamiltonian ($\hat{\mathcal{H}} = g_1\mu_B\mathbf{S}_1.\mathbf{B}_o + g_2\mu_B\mathbf{S}_2.\mathbf{B}_o - 2J_oh\mathbf{S}_1.\mathbf{S}_2$) was carried out using the MagProp analysis software within the DAVE suite.[27] Note that MagProp uses a convention of $-J_oh\mathbf{S}_1.\mathbf{S}_2$ for the exchange term, however it was normalized to the $-2J_oh\mathbf{S}_1.\mathbf{S}_2$ convention. The g values were constrained to be isotropic ($g_x = g_y = g_z$), and equivalent ($g_1 = g_2$).

EPR Spectroscopy

Instrumentation. Studies were performed at the EPR Facility of Arizona State University. Continuous wave (CW) EPR spectra were recorded between 4 K and 106 K using a Bruker ELEXSYS E580 CW X-band spectrometer (Bruker, Rheinstetten, Germany) equipped with a Model ESR900 liquid helium cryostat (Oxford Instruments, Oxfordshire, UK). The magnetic field modulation frequency was 100 kHz with a field modulation amplitude of 1 mT peak-to-peak. The microwave power was 1 mW, the microwave frequency was 9.44 GHz, and the sweep time was 168 seconds.

Spin Hamiltonian. The EPR spectra of a coupled dimer system can be described with the spin Hamiltonian:[28]

$$\mathcal{H} = -2J_oh\mathbf{S}_1.\mathbf{S}_2 + h\mathbf{S}_1.\mathbf{J}.\mathbf{S}_2 + \mathcal{H}_1 + \mathcal{H}_2 \qquad (6)$$

where J_o is the isotropic exchange coupling constant between the two Mn(II) ions of the dimer, $\mathbf{J}$ is the tensor describing the dipole-dipole interaction between the two Mn(II) spin centres, both in frequency units, h is Planck's constant, and $\mathcal{H}_i$ (i = 1, 2) are the spin Hamiltonians corresponding to each individual Mn(II) ion. The spin Hamiltonian of each Mn(II) spin centre contains the electron Zeeman interaction with the applied magnetic field $\mathbf{B}_o$, the zero-field interaction, and the hyperfine coupling interaction with the nucleus of ^{55}Mn:

$$\mathcal{H}_i = \mu_B\mathbf{S}_i.\mathbf{g}_i.\mathbf{B}_o + h\mathbf{S}_i.\mathbf{d}_i.\mathbf{S}_i + h\mathbf{S}_i.\mathbf{a}_i.\mathbf{I}_i \qquad (7)$$

where $\mathbf{S}_i$ and $\mathbf{I}_i$ are the electron and nuclear spin operators, respectively, $\mathbf{d}_i$, and $\mathbf{a}_i$ are the zero-field splitting and hyperfine coupling tensors, respectively, all in frequency units, $\mathbf{g}_i$ is the electronic g-tensor, and μ_B is the electron magneton. For Mn(II) dimers, the electron and nuclear spins of each Mn(II) ion are $S_i = 5/2$ and $I_i = 5/2$, respectively. Mn(II) ions have a singlet orbital ground state (^{6}A), with the first excited orbital state (^{4}T) more than 10,000 cm^{-1} above the ground state. Consequently, the zero-field energies of Mn(II) ions are generally small, $|D_i| < 0.1$ cm^{-1}.[29,30] For dimeric manganese complexes, the bridging atoms typically give a Mn–Mn exchange interaction that is significantly larger than 0.1 cm^{-1}. In this strong exchange regime, the isotropic exchange coupling energy is much larger than the electronic Zeeman energy ($|J_o| \gg g_i\mu_BB_o/h$) and the zero-field splitting ($|J_o| \gg |D_i|$). The dimer system may then be regarded as a ladder of isolated spin manifolds. These spin manifolds have total spin quantum numbers of $S = 0, 1, 2, 3, 4,$ and 5, each with a degeneracy of ($2S+1$). The energy separation between the spin manifolds is much larger than the microwave energy ($h\nu$) at the X-band (9.40 GHz) frequency and no transitions are observable between spin manifolds. The

individual spin manifolds can be considered independently and their corresponding spectra can be simulated using a spin Hamiltonian for each individual spin manifold given by:[31]

$$\mathcal{H}_S = \mu_B\mathbf{S}.\mathbf{G}_S.\mathbf{B}_o + h\mathbf{S}.\mathbf{D}_S.\mathbf{S} + h\mathbf{S}.\mathbf{A}_1.\mathbf{I}_1 + h\mathbf{S}.\mathbf{A}_2.\mathbf{I}_2 \qquad (8)$$

where $\mathbf{G}_S$, $\mathbf{D}_S$ and $\mathbf{A}_i$ (i = 1, 2) are the electronic Zeeman, zero-field splitting, and hyperfine coupling tensors, respectively, of the spin manifolds of the coupled system, and $\mathbf{S}$ is the spin operator of the coupled spin manifolds. The parameters of the coupled spin system can be expressed as linear combinations of the parameters of the individual spin centers:

$$\mathbf{G}_S = c_1\mathbf{g}_1 + c_2\mathbf{g}_2 \qquad (9)$$

$$\mathbf{D}_S = d_1\mathbf{d}_1 + d_2\mathbf{d}_2 + d_{12}\mathbf{J} \qquad (10)$$

$$\mathbf{A}_i = c_i\mathbf{a}_i \qquad (11)$$

where the coefficients c_1, c_2, d_1, d_2, and d_{12} are specific to the particular spin manifold and have been tabulated elsewhere.[40] For Mn(II) ions, the contributions from spin–orbit coupling to the g_i tensor and hyperfine coupling tensor are small, thus we will assume that both tensors $\mathbf{g}_i$ and $\mathbf{A}_i$ are isotropic. In the complex studied here, the two manganese centres of the dimer have identical ligation. The coordination geometry of one manganese ion is related to the other by a mirror plane, thus, we assume $g_1 = g_2 = g_{iso}$, $a_1 = a_2 = a$, and $\mathbf{d}_1 = \mathbf{d}_2$. In this study, hyperfine couplings due to Mn(II) were not explicitly included in the spin Hamiltonian (Eq. 8) since they were not well resolved in most of the experimental spectra. Furthermore, the individual spin manifolds do not contribute equally to the resulting spectrum at a particular temperature, T, because of their different Boltzmann populations. For antiferromagnetic isotropic exchange coupling (i.e. $J_o < 0$), the coefficient describing the Boltzmann population of an individual spin manifold S at thermal equilibrium and zero field is given by:[31]

$$n_S(J_o,T) = (2S+1)\exp[hS(S+1)J_o/kT]/Z \qquad (12)$$

where k is Boltzmann's constant and Z is the partition function defined by:

$$Z = 1 + 3\exp(2hJ_o/kT) + 5\exp(6hJ_o/kT) + 7\exp(12hJ_o/kT) + 9\exp(20hJ_o/kT) + 11\exp(30hJ_o/kT) \qquad (13)$$

Equation 12 shows that at very low temperature ($kT \ll |J_o|$) only the $S = 0$ spin manifold is populated, and consequently no EPR signal is observed. Upon increasing the temperature, the other spin manifolds gradually become populated and contribute to the EPR spectra. At high temperature ($kT \gg |J_o|$), a superposition of signals, originating from all spin manifolds, is observed.

Fitting of EPR spectra. To quantitatively compare experimental and simulated spectra, we divided the spectra into N intervals (i.e., we treated the spectrum as an N-dimensional vector $\mathbf{R}$). Each component R_j has the amplitude of the EPR signal at a magnetic field B_j, with j varying from 1 to N. The amplitudes of the experimental and simulated spectra were normalized so that the span between the maximum and minimum values of R_j

is 1. We compared the calculated amplitudes R_j^{calc} of the signal with the observed values R_j defining a root-mean-square deviation by:

$$\sigma(p_1, p_2,..., p_n) = [\Sigma(R_j^{calc}(p_1, p_2, ..., p_n) - R_j^{exp})^2/N]^{\frac{1}{2}} \qquad (14)$$

where the sums are over the N values of j, and p's are the fitting parameters that produced the calculated spectrum. For our simulations, N was set equal to 2048. The EPR spectra were simulated using EasySpin (v 5.2.25), a computational package developed by Stoll and Schweiger[32] and based on Matlab (The MathWorks, Natick, MA, USA). EasySpin calculates EPR resonance fields using the energies of the states of the spin system obtained by direct diagonalization of the spin Hamiltonian (see Eq. 8). The EPR fitting procedure used a Monte Carlo type iteration to minimize the root-mean-square deviation, σ (see Eq. 14) between measured and simulated spectra. We searched for the optimum values of the following parameters: the isotropic g-value (g_{iso}), the zero-field splitting parameters (D and E), the principal components of the J tensor ($J_{x'}$, $J_{y'}$ and $J_{z'}$) and the isotropic peak-to-peak linewidth (ΔB).

Preparation of [($^{2,6-iPr2Ph}$BDI)Mn(μ-OH)]$_2$ (6). A 20 mL vial was charged with **1** (117.1 mg, 0.1237 mmol) dissolved in 10 mL THF and cooled to 238 K. A solution of H_2O (4.5 μL, 0.247 mmol) in 5 mL THF was cooled at 238 K. After 30 minutes, the H_2O solution was added dropwise to the solution of **1** while stirring. A colour change from yellowish-orange to light yellow was noticed along with the liberation of H_2 gas. Then, the mixture was filtered through Celite, and the solvent was removed under vacuum to obtain a yellow solid. The solid was washed thoroughly with Et_2O and recrystallized from THF upon cooling to 238 K, affording yellow crystals of **6** (37.8 mg, 0.038 mmol). The Et_2O wash was also cooled to 238 K, affording an additional quantity of **6** (13.4 mg, 0.0136 mmol). The total yield was 42%. The deuterated variant, [($^{2,6-iPr2Ph}$BDI)Mn(μ-OD)]$_2$ (**6-d_2**), was prepared in a similar fashion using D_2O. Elemental analysis for $C_{58}H_{84}O_2N_4Mn_2$: Calcd. C, 71.14; H, 8.65; N, 5.72. Found: C, 70.35; H, 8.76; N, 5.94. Magnetic susceptibility (Gouy method, 291 K): μ_{eff} = 7.4 μ_B (considering a dimeric structure). Infrared (KBr): υ_{OH} = 3,695 cm^{-1}, υ_{OD} = 2,726 cm^{-1}.

Results and Discussion

In 2005, Roesky et al. reported a dimeric analogue of **1** which lacks hydride ligands, [($^{2,6-iPr2Ph}$BDI)Mn]$_2$ (Fig. 2).[11] Notably, single crystal X-ray diffraction analysis of this compound revealed staggered BDI ligands and a Mn–Mn distance of 2.7206(5) Å. Instead of having a $3d^6$ configuration, the Mn(I) centres of this complex adopt a $4s^13d^5$ configuration, enabling the $4s$ orbitals from each metal centre to form a single bond. Further information about the ground state and magnetism of [($^{2,6-iPr2Ph}$BDI)Mn]$_2$ was gathered by DFT analysis;[11] however, the reason for this compound's absence of Mn–Mn multiple bonding had not been interrogated.
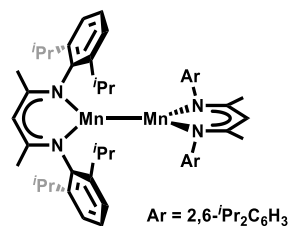

Fig. 2 The dimeric manganese complex, [($^{2,6-iPr2Ph}$BDI)Mn]$_2$, reported by Roesky and co-workers.[10]

In 2018, it was determined that the solid-state structure of **1** features eclipsed, rather than staggered BDI ligands.[8] Given the formal oxidation state and structural differences between [($^{2,6-iPr2Ph}$BDI)Mn]$_2$ and **1**, we began this investigation by exploring the electronic structure of a dicationic Mn dimer that lacks hydride ligands, but features eclipsed BDI chelates. Fig. 3a shows a simplified MO diagram of the conceptual complex, [($^{2,6-iPr2Ph}$BDI)Mn]$_2^{2+}$. For this dimer, the in-phase combinations of the d_{xy}, d_{xz}, and $d_{x^2-y^2}$ orbitals could interact to form a Mn–Mn triple bond. The bonding, non-bonding, and antibonding combinations of the d_{z^2} and d_{yz} orbitals are expected to be nearly degenerate, giving rise to four unpaired electrons.

In turn, this diagram forms the basis of the conceptual molecular orbital diagram of **1**, which is shown in Fig. 3b. For **1**, the in-phase combination of the d_{xy} orbitals is expected to interact with the out-of-phase combination of the hydride s-orbitals. After taking the bridging hydride ligands into account, four unpaired electrons remain in the weakly interacting d_{z^2} and d_{yz} orbitals. Importantly, the frontier molecular orbital diagram in Fig. 3b is consistent with the previously reported solution magnetic susceptibility of **1** (5.2 μ_B at 298 K).[8] The electrons initially expected to contribute to a bonding interaction between the metal centres (as shown in Fig. 3a) are instead redistributed into Mn–H bonding as illustrated in Fig. 3b. This σ-bonding interaction is speculated to reduce the bond order between the manganese centres to between 2 and 3. The crystal structure of **1**, however, revealed a Mn–Mn distance of 2.8138(7) Å,[8] which is significantly longer than the bond length expected for a Mn–Mn triple bond.[33,34] Manganese dimers reported to feature triple bonds possess Mn–Mn distances of approximately 2.2 Å,[35,36] suggesting that the bond order between the Mn centres of **1** is considerably lower than 3.
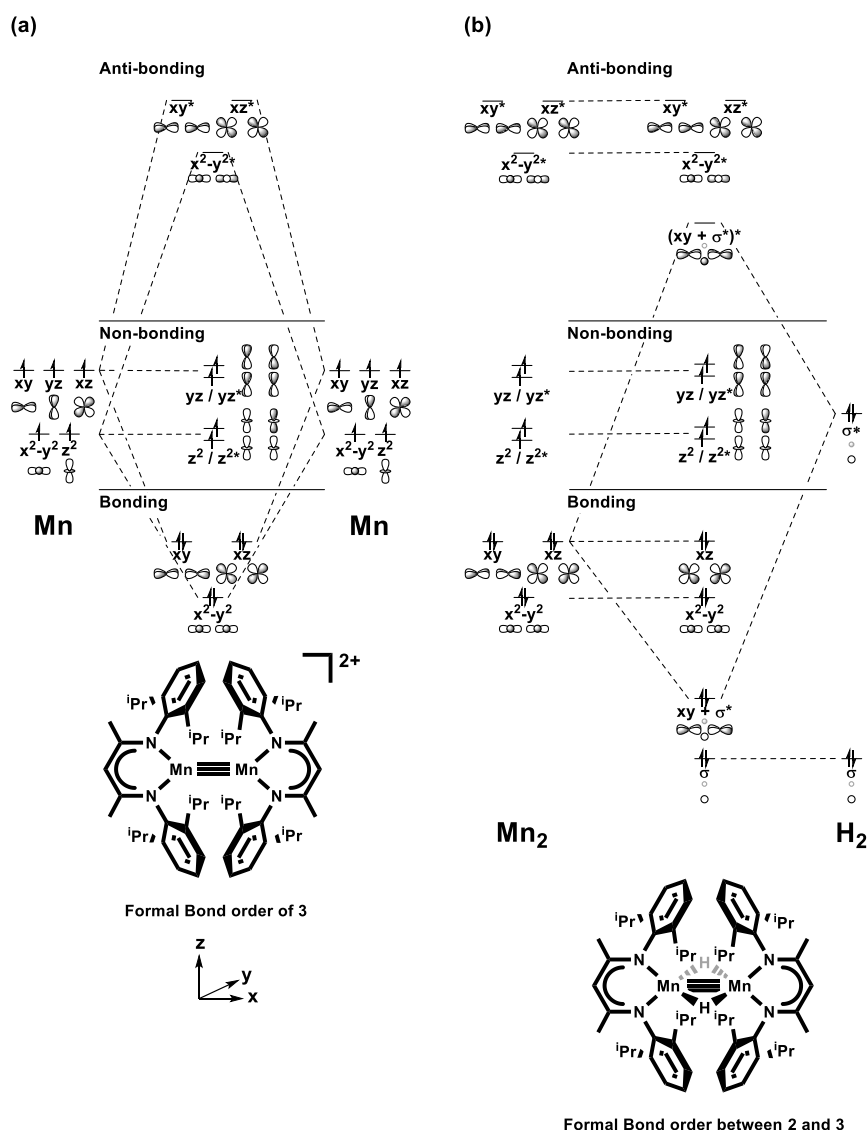
(a)   **(b)**

Fig. 3 Conceptual MO diagrams for (a) $[(^{2,6\text{-}iPr2Ph}BDI)Mn]_2^{2+}$ and (b) **1**, which features an interaction between the out-of-phase hydride combination and the in-phase d_{xy} orbital combination.

The X-band (9.4 GHz) electron paramagnetic resonance (EPR) spectrum of **1** was also reported in 2018.[8] At 106 K, a superposition of three spin states, $S = 1$, $S = 2$, and $S = 3$, was observed. Spectral analysis revealed that the two Mn(II) centres are high-spin and antiferromagnetically coupled to one another. Computationally, we found that the ground state of **1** is the broken-symmetry $S = 0$ state, and the electronic energy of the $S = 5$ state is higher than that of the $S = 0$ state by only 0.9 kcal/mol, implying that higher spin states are thermally accessible. Consequently, the spin states in between the two extreme states, $S = 1$, $S = 2$, $S = 3$, and $S = 4$ states, can be accessed under the conditions of the EPR experiment. The ambient temperature solution effective magnetic moment of **1** (5.2 μ_B) is therefore the ensemble average value of the states accessible at room temperature, rather than an indication of a strictly $S = 2$ state. Therefore, computational models with ferromagnetic ($S = 5$, **1-F**) and antiferromagnetic coupling (broken-symmetry $S = 0$, **1-AF**) between the metal centres,

representing the extreme states, were selected for further evaluation.

The optimized geometries of **1-F** and **1-AF** are in good agreement with the crystal structure (**1-CS**),[8] as shown in Table 1. The computed Mn–Mn distances are 2.871 Å for both **1-F** and **1-AF**, which is comparable to that of the crystal structure, 2.814 Å. The pseudo-tetrahedral geometry around the Mn centres and the eclipsed positioning of the β-diketiminate ligands were clearly reproduced. Fig. 4 highlights the structural consistency between the X-ray crystallographic data and the optimized geometries of **1-F** and **1-AF**. The absence of a multiple bond between the manganese centres was observed, with Mayer bond orders of 0.21 and 0.27 for **1-F** and **1-AF**, respectively.
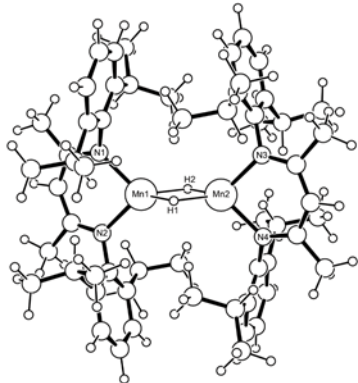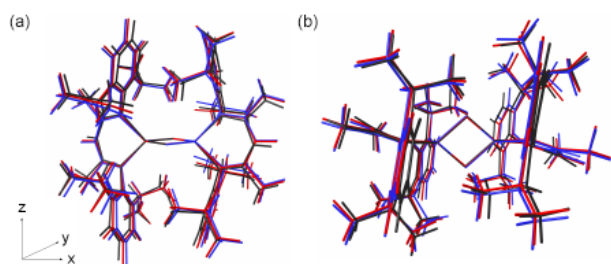
Fig. 4 Overlay of the structures of **1-CS** in black, **1-F** in blue, and **1-AF** in red: (a) the xz-plane view and (b) the orthogonal view along the z-axis.

To further interrogate the lack of a Mn–Mn multiple bond, the MO-diagrams of **1-F** and **1-AF**, shown in Fig. 5, were analysed. The MO-diagrams were simplified by adopting a local D_{2h} symmetry. In total, 12 MOs comprising 10 metal-based orbitals and 2 hydride-based orbitals are presented. As expected, the in-phase combination of the d_{xy} orbitals interacts with the out-of-phase combination of hydride orbitals to afford a bonding and antibonding combination for both **1-F** and **1-AF**. Furthermore, an interaction between the bonding combination of the d_{z^2} orbitals and the in-phase combination of hydride orbitals is observed, generating a low-lying bonding orbital and high-lying antibonding orbital.

The left-hand side of Fig. 5 illustrates the **1-F** MOs. The β-orbitals of **1-F** are higher in energy than the corresponding α-orbitals due to the absence of exchange interaction.[37,38] On the other hand, both spin orbitals are paired up in **1-AF**, with MOs derived from Noodleman's broken-symmetry approach (Fig. 5, right). Interestingly, the metal d_{xz} orbitals are higher in energy than expected. Isosurface plots of the in-phase and out-of-phase combinations of the d_{xz} orbitals are shown in Fig. S2. The metal d_{xz} orbitals are mixed with BDI-based orbitals via σ-bonding. Importantly, the ligand-based orbitals are antibonding with respect to the metal-based orbitals, destabilizing the MOs.

The corresponding bonding combinations are much lower in energy and not depicted. These bonding combinations between the BDI ligand and Mn centres are ultimately responsible for the low Mayer bond orders determined for **1-F** and **1-AF**.

Table 1 Optimized structural parameters of the dimanganese complexes **1-F**, **1-AF** and **1-CS**

	1-F	**1-AF**	**1-CS**
	calc.	calc.	exp.
Spin-Coupling	F	AF	–
Mn1–H1 (Å)	1.897	1.834	1.791
Mn1–H2 (Å)	1.919	1.923	1.938
Mn1–N1 (Å)	2.099	2.103	2.086
Mn1–N2 (Å)	2.116	2.110	2.098
∠H1–Mn1–N2 (°)	116.9	120.5	121.1
∠N2–Mn1–N1 (°)	90.1	90.5	91.5
∠N1–Mn1–H2 (°)	121.9	119.8	118.3
∠H2–Mn1–H1 (°)	82.2	80.5	82.1
τ₄ Mn1	0.86	0.85	0.85
Mn1–Mn2 (Å)	2.871	2.871	2.814
∠Mn1–H1–Mn2 (°)	97.5	99.6	97.9
Spin-Densities[a] Mn1	4.91	4.75	–
Spin-Densities[a] Mn2	4.91	–4.75	–
Mayer Bond Order for Mn–Mn	0.21	0.27	–
Relative Escf[b] (kcal mol⁻¹)	0.90	0	–

[a]Mulliken spin-density.
[b]The relative energies (kcal mol⁻¹) are referenced to the AF-coupled state.
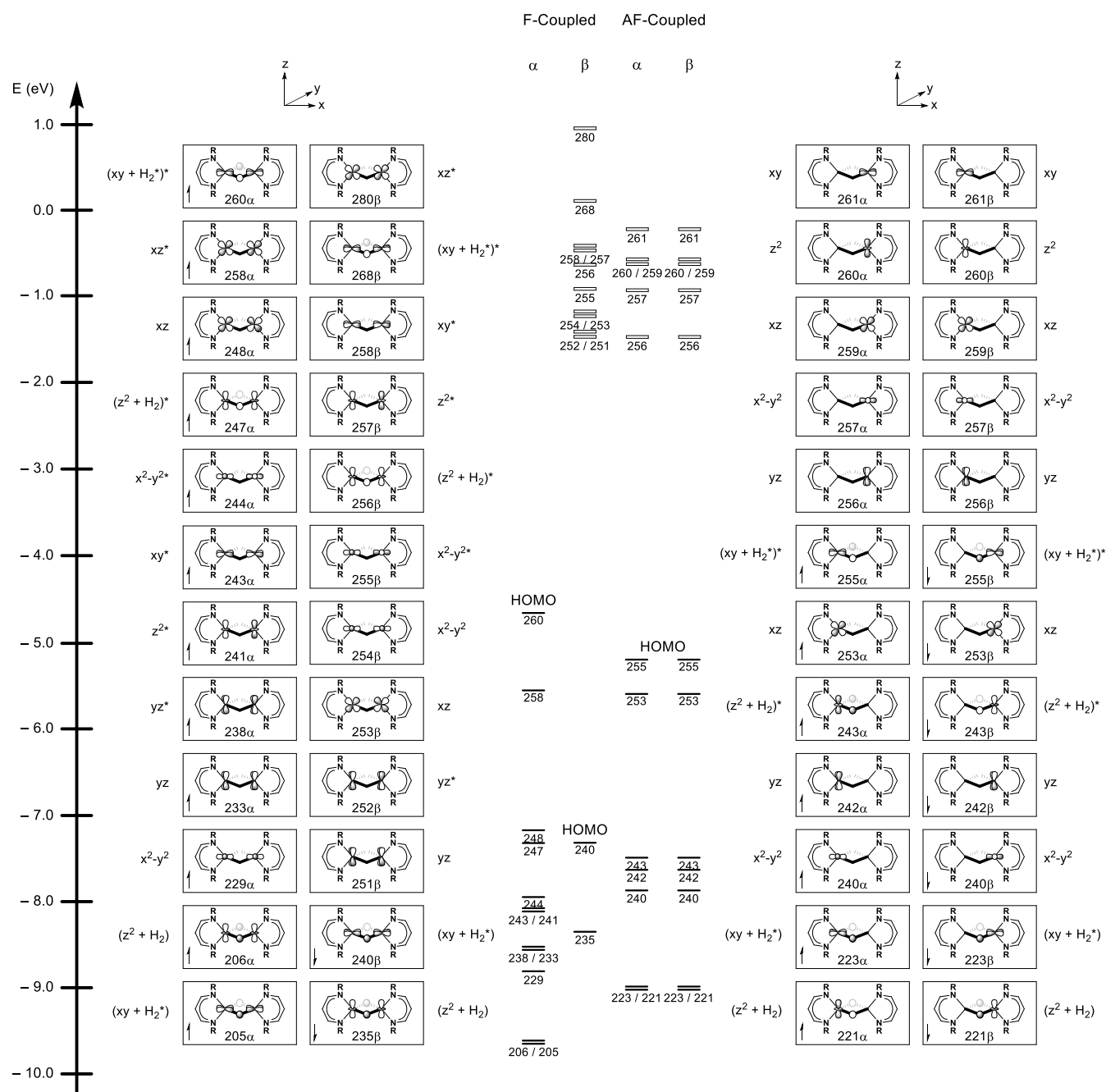
Fig. 5 MO-diagrams of ferro- (**1-F**) and antiferromagnetically-coupled (**1-AF**) Mn centres in **1**.

Determination of J_o for **1**.

According to Noodleman's broken-symmetry orbital method, the Heisenberg exchange coupling constant, J_o, can be directly calculated from the energy difference between a high-spin state and a broken-symmetry state.[24] In the broken-symmetry approach, the energy difference between the high-spin state and the broken-symmetry state is:

$$E(S_{max}) - E(BS) = -S_{max}(S_{max} + 1) \cdot J_o \qquad (15)$$

where S_{max} is the maximum number of unpaired electrons per monomeric unit. Here, each manganese centre has five unpaired d-electrons; therefore, the high-spin state is a sextet. The coupling constant is sensitive to the distance between metal centres, as well as the number of electrons shared by the metal centres. Therefore, probing J_o values will be the best way to assess the interaction between the Mn centres of **1**. Using equation (15) the Heisenberg exchange coupling constant was determined to be −10.9 cm⁻¹. This is an order of magnitude lower than the J_o-value of −110 cm⁻¹ determined for [($^{2,6-iPr2Ph}$BDI)Mn]₂ by Roesky and co-workers using the B3LYP functional.[11] Jones and co-workers synthesized a similar compound, (L*Mn)₂ (L* = -N(AR*)SiMe₃)), which also shows a single Mn–Mn bond arising from σ-interactions.[39] The calculated J_o-value reported by the Jones group was −47.5 cm⁻¹, which is still stronger than the one calculated here.

The broken-symmetry approach does not distinguish between direct magnetic exchange interactions and indirect magnetic exchange interactions, such as superexchange. Bridging hydrides are capable of mediating strong superexchange interactions between metal centres due to the small size of the ion and the symmetry of the *s*-orbital. Calculating superexchange explicitly with DFT requires the use of a multi-reference calculation, such as Complete Active Space SCF (CASSCF),[40] which is computationally expensive for a complex of the size of **1**. Nevertheless, it is expected that the superexchange is at least partially responsible for the calculated J_o value of -10.9 cm^{-1}.

With a computed J_o value in hand, attempts were made to determine this value using two complementary experimental techniques. In our initial contribution, **1** was found to exhibit an ambient temperature magnetic moment of 5.2 μ_B at 298 K (Evans Method);[8] however, variable temperature data had not been collected. Therefore, a sample of **1** was analysed by SQUID magnetometry between 1.8–300 K. The solid-state χT value of **1** was found to be 4.5 cm^{3}K/mol (6 μ_B) at room temperature, which is significantly below the spin-only value for two non-interacting S = 5/2 Mn(II) centres (χT_{SO} = 8.75 cm^{3}K/mol). This observation is indicative of antiferromagnetic coupling between the Mn centres, a multiply-bonded complex with a lower overall spin state, or some intermediate case. Upon cooling, the χT of **1** decreases, indicative of antiferromagnetic coupling (Fig. 6). A similar plot was observed under an applied field of 1.0 T, and a significant increase of χT was noted after the sample was allowed to oxidize.
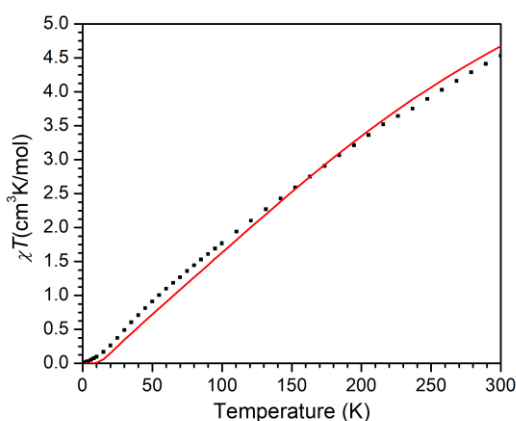
resulted in a slightly poorer, but still reasonable fit with $J_o = -20$ cm^{-1} ($\pm$ 0.1 cm^{-1}). The value of g is within error in both fits, providing a consistent J_o value of -15 to -20 cm^{-1}.

To determine the isotropic exchange coupling by X-band EPR spectroscopy, we carried out measurements of **1** at six different temperatures between 4 K and 106 K. Fig. 7a shows the temperature variation of the EPR intensity of the signals occurring around 180 mT (B_1) and 60 mT (B_2) (see Fig. 8b). The EPR signals at B_1 and B_2 belong to the S = 1 and S = 2 spin manifolds, respectively. They were identified by simultaneously simulating the EPR spectra of **1** at different temperatures. At 4 K (Fig. 7b), the spectrum was simulated considering a superposition of two spin manifolds, S = 1 and S = 2. The parameters used to fit the EPR spectra of **1** (see Experimental Section) were within experimental error of our previously reported parameters.[8] The value of J_o can be obtained by fitting the experimental data in Fig. 8a using Eq. 13 (see Experimental Section) which accounts for the Boltzmann populations of the energy levels associated with the S = 0, S = 1, S = 2, S = 3, S = 4 and S = 5 spin manifolds. A value of -9.5 cm^{-1} was obtained when all data points were included in the fit. If the data point corresponding to the EPR signal at B_1 and measured at 80 K is not included in the fit (see Fig. 8 caption for details), a value of -10.8 cm^{-1} was obtained. Using the average of the two values, we determined from the temperature dependence of the X-band EPR spectrum of **1** that $J_o = -10.2 \pm 0.7$ cm^{-1}. Considering the SQUID and EPR data, our experimental efforts to determine J_o are consistent with weak antiferromagnetic coupling between the Mn centres of **1**.
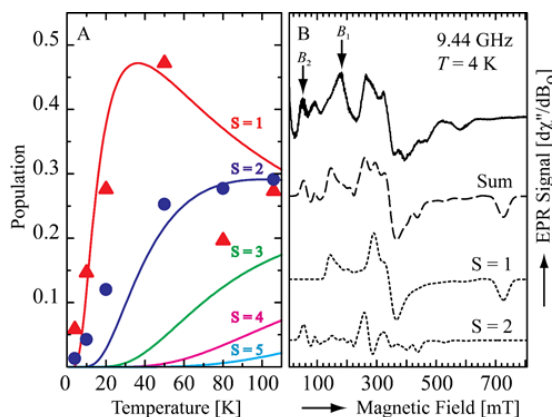

Fig. 6 Temperature-dependent χT vs. T data for **1** collected under an applied field of 0.1 T. The red line is the fit where g is fixed at 2.05, as outlined in the text.

The data collected at 0.1 T was modelled using the DAVE program.[27] The two Mn centres of **1** were treated as isotropic, spin-only (S_{Mn} = 5/2) centres, and presumed to be identical given their crystallographic equivalence. The best fit was acquired with a g-value of 1.82 ($\pm$ 0.25) and an antiferromagnetic J_o coupling of -15 cm^{-1} ($\pm$ 0.1 cm^{-1}, normalized to $2J_o$ convention). Constraining the fit to the g value of 2.05 previously determined by EPR spectroscopy

Fig. 7 (a) Signal intensity times temperature as a function of temperature for the EPR signals around 180 mT (B_1) (red triangles) and 60 mT (B_2) (blue circles) present in the EPR spectra of **1**. Temperature dependence of Boltzmann populations corresponding to S = 1 (red line), S = 2 (blue line), S = 3 (green line), S = 4 (magenta line) and S = 5 (cyan line) spin manifolds. These curves were calculated using Eq. 12 with the value of J_o that best fits the available experimental data. It can be noticed that the population corresponding to the EPR signal at B_1 and measured at 80 K deviates significantly from the fit. (b) The X-band EPR spectrum of **1** at 4 K. The solid line is the experimental spectrum, and the dashed line is the sum of the simulated spectra for S = 1 and S = 2 dimer spin states (dotted

ARTICLE

lines). The EPR signals marked with arrows as B_1 and B_2 were identified as originating from the $S = 1$ and $S = 2$ dimer spin states, respectively. This spectrum did not show well-resolved [55]Mn hyperfine couplings. However, multiline patterns corresponding to the hyperfine couplings (~3.6 mT) of two equivalent Mn(II) ions were observed in the EPR spectrum at 20 K (not shown).

Influence of steric bulk.

A reasonable hypothesis is that the sterically bulky BDI ligands of **1** preclude the formation of a metal–metal multiple bond as described in the literature.[8,11,25,39] Bulky groups attached to the β-diketiminate ligand may sterically prohibit the proximal positioning of two metal centres, despite being within range of interaction.[41] In this regard, the lower than anticipated bond order between the metal centres could be attributed to steric hindrance. To evaluate this proposition, a model compound supported by the most sterically-simplified version of the β-diketiminate ligand was modelled, for which all substituents are replaced with hydrogen atoms. Fig. 8 depicts the model compound, **2**.

Calculations on **2** reproduced a nearly identical MO diagram to that of the full compound, **1**, as depicted in Fig. S1. The Mn–Mn bond lengths of the model compound were calculated to be 2.816 and 2.789 Å for **2-F** and **2-AF**, respectively (Table 2). Therefore, the Mn centres of **1-F** and **1-AF** are only 0.06 Å and 0.08 Å farther apart than the same states of **2**, suggesting that steric effects minimally influence Mn-Mn bonding. The corresponding Mayer bond orders of 0.21 and 0.24 for **2-F** and **2-AF** are comparable to the bond orders of 0.21 and 0.27 for **1-F** and **1-AF**.
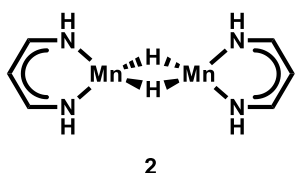

Fig. 8 The model compound **2**.

The irrelevance of chelate steric hindrance allows us to consider the fundamental basis for the absence of Mn-Mn multiple bonding in **2**. Interaction between the metal d-orbitals and ligand-based orbitals appears to be the intrinsic reason for an unexpectedly low Mn–Mn bond order. The β-diketiminate ligand has a bite angle of around 90° (Table 1 and 2) and a conjugated π-system, which affords thorough mixing between the metal- and ligand-based orbitals. As previously mentioned for **1**, the d_{xz} orbitals of **2** are mixed with the orbitals of the nitrogen atoms of the β-diketiminate ligands (Fig. S3). The metal d_{xy} orbitals also interact with the β-diketiminate-based orbitals, as well as with the hydride-based orbitals (Fig. S4). Electrons that are supposed to occupy bonding orbitals between the metal centres are dispersed to these metal–ligand interactions, resulting in attenuation of metal–metal bonding.

Despite adopting the broken-symmetry approach, the d_{xy} and d_{z^2} orbitals contain delocalized counterparts (Fig. S4 and

Fig. S5). Considering weak δ-interactions with the d_{z^2} orbitals, we posited that the Mn–Mn bond order of around 0.2 is mainly attributed to the d_{xy} orbitals. The MO diagram for the ferromagnetically coupled state, **2-F**, advocates for this postulation (Fig. S1). The α-orbitals consist of bonding and antibonding pairs of orbitals that compensate for each other. The remaining β-orbital bonding combinations coincide with the d_{xy} and d_{z^2} orbitals in the antiferromagnetically-coupled state, which contain residual moieties on the Mn centres, as shown in Fig. S4 and Fig. S5. Furthermore, hydride s-orbitals are incorporated in the d_{xy} and the d_{z^2} orbitals, presumably indicating the presence of a superexchange interaction mediated by bridging hydrides.

Table 2 Comparison between optimized geometries of the full complex, **1**, and the model compound **2**

|	1-F	1-AF	2-F	2-AF
Spin-Coupling	F	AF	F	AF
Mn1–H1 (Å)	1.897	1.834	1.889	1.847
Mn1–H2 (Å)	1.919	1.923	1.894	1.856
Mn1–N1 (Å)	2.099	2.103	2.069	2.067
Mn1–N2 (Å)	2.116	2.110	2.069	2.067
∠H1–Mn1–N2 (°)	116.9	120.5	121.9	121.6
∠N2–Mn1–N1 (°)	90.1	90.5	91.4	91.5
∠N1–Mn1–H2 (°)	121.9	119.8	120.7	121.1
∠H2–Mn1–H1 (°)	82.2	80.5	83.7	82.3
τ₄ Mn1	0.86	0.85	0.83	0.83
Mn1–Mn2 (Å)	2.871	2.871	2.816	2.789
∠Mn1–H1–Mn2 (°)	97.5	99.6	96.2	97.7
Spin-Densities[a] Mn1	4.91	4.75	4.87	4.73
Spin-Densities[a] Mn2	4.91	−4.75	4.87	−4.73
Mayer Bond Order for Mn–Mn	0.21	0.27	0.21	0.24
Relative E$_{SCF}$[b] (kcal mol⁻¹)	0.90	0	4.24	0

[a]Mulliken spin-density.

[b]The relative energies (kcal mol⁻¹) are referenced to the AF-coupled states.

Extension to ligands with *p*-orbitals.

The nitrile dihydroboration activity of **1** was recently reported by our groups.[9] The proposed mechanism involves a Mn(II) intermediate similar to **1**, [($^{2,6-iPr2Ph}$BDI)Mn(μ-NCHC₆H₅)]₂, in which bridging hydrides are replaced with bridging imino(amide) groups. While **1** is lower in energy than hydride monomers by only 1.5 kcal/mol, the dimeric intermediate with bridging imines is more stable than its respective monomers by 22.51 kcal/mol. It also features an elongated Mn–Mn distance of 3.082 Å (vs. 2.814 Å for **1**). This difference can be attributed to a fundamental difference in orbital interactions. The bonding combination between the metal centres of **2** occurs through bridging hydride ligands. Spherical hydride 1s-orbitals allow the in-phase combination of metal d-orbitals, while bridging ligands that feature p-orbitals have a node that precludes bonding interactions between the Mn centres. Only th out-of-phase combination

will be allowed with p-orbitals present. To gain further insight, interactions between the Mn centres were investigated upon substituting bridging fluoride and hydroxide ligands for the bridging hydrides of **2**. The respective model compounds **3** and **4** are shown in Fig. 9.

Fig. 9 Model compounds featuring bridging ligands with p-

| 3 | 4 |
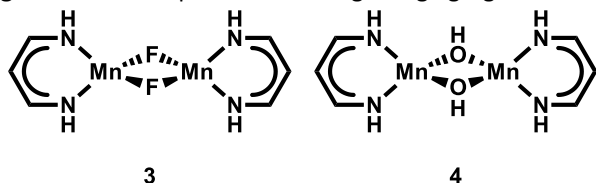
orbital character.

The most remarkable difference is the elongated Mn–Mn distance from 2.789 Å (for **2-AF**) to 3.074 Å and 3.100 Å in conjunction with the decrease in Mayer bond order from 0.24 (for **2-AF**) to 0.02 and 0.03 in **3** and **4**, respectively. For each compound, analogous patterns for mixing metal- and BDI ligand-based orbitals were observed. For compounds **3** and **4**, all metal d-orbitals were mixed with bridging atom p-orbitals, implying that the degree of Mn–Mn interaction is decreased. The d_{xy} orbitals, which were responsible for M-M bonding in **2**, are depicted in Fig. S6 and Fig. S7 for **3** and **4**, respectively. The p_x and p_y orbitals are mixed to interact with the d_{xy} orbitals, simultaneously accounting for monoanionic and lone pair interactions. Bonding interactions between the metal centres via bridging ligands are symmetry forbidden for **3** and **4**. As a consequence, Mn–Mn bond strength is attenuated, resulting in an increased Mn–Mn distance.

Table 3 Comparison of structural parameters of the optimized geometries of the model compounds **2**, **3**, and **4**

	2	3	4
Spin-Coupling	AF	AF	AF
Mn1–H1(O1, F1) (Å)	1.847	2.019	2.043
Mn1–H2(O2, F2) (Å)	1.856	2.019	2.043
Mn1–N1 (Å)	2.067	2.076	2.101
Mn1–N2 (Å)	2.067	2.077	2.102
∠H1(O1, F1)–Mn1–N2 (°)	121.6	121.8	130.0
∠N2–Mn1–N1 (°)	91.5	92.4	90.6
∠N1–Mn1–H2(O2, F2) (°)	121.1	121.7	122.6
∠H2(O2, F2)–Mn1–H1(O1, F1) (°)	82.3	80.8	81.3
τ₄ Mn1	0.83	0.82	0.76
Mn1–Mn2 (Å)	2.789	3.074	3.100
∠Mn1–H1(O1, F1)–Mn2 (°)	97.7	99.2	98.7
Spin-Densities* Mn1	4.73	4.81	4.80
Spin-Densities* Mn2	−4.73	−4.81	−4.80
Mayer Bond Order for Mn–Mn	0.24	0.02	0.03

*Mulliken spin-density.

Lone pair donation presumably accounts for the stabilization effect observed for *p*-orbital bridged compounds.

Table 4 describes the fragment analysis of the three model compounds, **2**, **3**, and **4**. The compounds were fragmentized in three parts, one manganese subunit, the other manganese subunit, and the bridging ligands. Large electron densities located on the bridging anions give rise to an immense repulsion in the core composed of the Mn centres and bridging ligands. Due to the enlarged core structure of **3**, the Pauli repulsion term is decreased by 22.5 kcal/mol compared to **2**. On the contrary, the elongated Mn–Mn distance decreases the extent of electrostatic interaction in **3**; however, the electrostatic terms do not exceed the repulsion terms, rendering **3** more stable than **2**.

At first glance, the computed interaction components of **4** seem contradictory, but they can be explained. Hydroxides are much larger than hydrides; therefore, the Pauli repulsion term of **4** is 10.0 kcal/mol higher than that of **2**. Electrostatic interactions are understandably strengthened. Consequently, the degree of stabilization through non-orbital interactions in **3** and **4** is nearly identical. Despite the longer distances, the magnitude of p-orbital interaction in **3** and **4** is greater than the s-orbital interaction in **2**. The penalties in non-orbital and orbital interactions of **2** give rise to electronic destabilization. Dimerization involves a stabilization in enthalpy and disadvantage in entropy. The penalties in interaction terms of **2** can partially offset the stabilizing effect in enthalpy of the dimerization. As a result, the electronic energy of the dimer is lower by 32.5 kcal/mol than that of two equivalents of the corresponding monomer in the case of **2**, while **3** and **4** show greater energy differences of 41.9 and 50.0 kcal/mol, respectively. Considering entropy penalties, the monomer-dimer Gibbs energy differences in **2**, **3**, and **4** at room temperature diminish to 18.6, 28.3, and 35.8 kcal/mol, respectively. Furthermore, in benzene, the energy difference at room temperature of **2** becomes 4.1 kcal/mol, while that of **3** and **4** stays at 16.5 and 24.6 kcal/mol, which is far more challenging to attain. Notably, the full fluoride congener of **1**, [($^{2,6-iPr2Ph}$BDI)Mn(μ-F)]₂ (**5**), and the full hydroxide congener of **1**, [($^{2,6-iPr2Ph}$BDI)Mn(μ-OH)]₂ (**6**) are lower in energy than their corresponding monomers by 22.6 and 28.8 kcal/mol, respectively.

Table 4 Computed components for the interaction between the Mn centres and bridging ligands in **2**, **3**, and **4**

| 2 | 3 | 4 |

(in kcal/mol)	2	3	4	Δ₁ (3 − 2)	Δ₂ (4 − 2)
Mn–Mn (Å)	2.789	3.074	3.100	–	–
Pauli repulsion (PR)	278.93	256.47	288.91	−22.46	9.98
Electrostatic interaction (EI)	−618.85	−608.69	−639.48	10.16	−20.63
Non-orbital interaction (PR + EI)	−339.92	−352.22	−350.58	−12.30	−10.65
Orbital interaction	−395.21	−400.01	−431.05	−4.80	−35.84

Synthesis of the hydroxide-bridged dimer.

To support the calculations conducted on model compound **4** and full hydroxide complex **6**, attempts were made to synthesize the latter. Upon dissolving **1** in THF solution, the slow addition of a second THF solution containing two equivalents of H_2O resulted in the liberation of H_2 gas and a light-yellow product identified as **6**. The magnetic susceptibility of **6** was analysed by the Gouy method and determined to be 7.4 μ_B at 291 K. Notably, the infrared spectrum of this complex was found to exhibit a hydroxide OH stretch at 3,695 cm^{-1} that shifted to 2,726 cm^{-1} when D_2O was employed in the synthesis (**6**-d_2).

Single crystals of **6** were grown from THF at 238 K, and X-ray diffraction data were collected. The crystal structure of **6** (Fig. 10) features an inversion centre, eclipsed BDI ligands, and a relatively long Mn1–Mn1A distance of 3.1426(9) Å. This distance is consistent with the calculated distance of 3.189 Å, and a full comparison of the experimental and computational bond distances is provided in Table 5. Notably, the hydroxide hydrogen atoms were located in the difference map and were found to occupy the same location in two independent crystals.
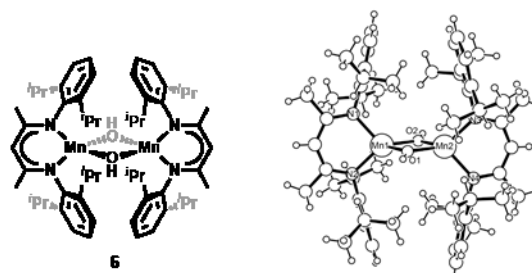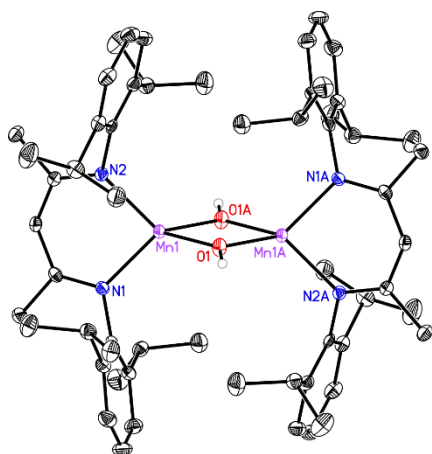

Fig. 10 Solid-state structure of **6** at 30% probability ellipsoids.‡

To obtain additional electronic information, a sample of **6** was analysed by SQUID magnetometry between 1.8–300 K (Fig. 11). At 298 K, the data reveals a χT value of 7.70 cm^{3}K/mol, which is lower than the spin-only value for two high-spin uncoupled Mn(II) centres (χT_{SO} = 8.75 cm^{3}K/mol). This χT value corresponds to an effective magnetic moment of 7.8 μ_B at ambient temperature, which is consistent with the magnetic susceptibility determined using the Gouy method at 291 K (7.4 μ_B). The best fit was obtained with a *g*-value of 1.94 and a weak antiferromagnetic coupling of J_o = −5 cm^{-1} (normalized to $2J_o$ convention). Interestingly, the magnitude of J_o value was only one wavenumber different when fitting the data to *g* = 2.05. The exchange coupling constant was calculated to be −4.3 cm^{-1}, which is in good agreement with the experimental data.

Table 5 Experimental and calculated metrical parameters of **6**

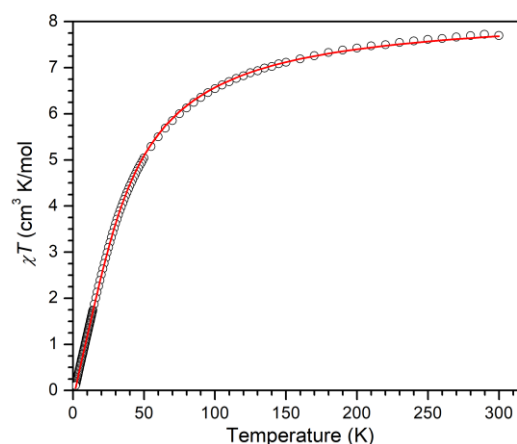|	6 exp.	6 calc.
Spin-Coupling	–	AF
Mn1–O1 (Å)	2.037	2.056
Mn1–O2 (Å)	2.054	2.071
Mn1–N1 (Å)	2.106	2.107
Mn1–N2 (Å)	2.108	2.119
∠O1–Mn1–N2 (°)	127.0	125.0
∠N2–Mn1–N1 (°)	91.3	89.2
∠N1–Mn1–O2 (°)	120.5	124.5
∠O2–Mn1–O1 (°)	79.6	78.9
τ₄ Mn1	0.80	0.78
Mn1–Mn2 (Å)	3.142	3.189
∠Mn1–O1–Mn2 (°)	100.4	101.2
Spin-Densities[a] Mn1	–	4.80
Spin-Densities[a] Mn2	–	−4.80

[a]Mulliken spin-density.

Fig. 11 Temperature-dependent χT vs. *T* data for **6** collected under an applied field of 0.1 T. The red line is the fit where *g* is fixed at 2.05.

Conclusions

A thorough electronic structure analysis of [($^{2,6\text{-}iPr2Ph}$BDI)Mn(μ-H)]$_2$ (**1**) revealed a lack of Mn-Mn bonding due to BDI-Mn orbital overlap. Therefore, **1** is best considered to be a 13-electron compound. Steric interactions between neighbouring BDI ligands were found to have little influence on the Mn-Mn Mayer bond order. When the hydride ligands of **1** are substituted for fluoride or hydroxide ligands, bridging atom *p*-orbital σ-bonding and lone pair interactions increase the Mn-Mn distance while weakening isotropic exchange coupling. The experimental data collected for [($^{2,6\text{-}iPr2Ph}$BDI)Mn(μ-OH)]$_2$ (**6**) supports this assessment.

This contribution holds implications for the utilization of related compounds as catalysts for organic transformations. For example, we now understand that the enhanced overlap afforded by the bridging nitrogen atom p-orbitals in [($^{2,6\text{-}iPr2Ph}$BDI)Mn(μ-NCHC$_6$H$_5$)]$_2$ render this resting state 16.9 kcal/mol more stable than the corresponding monomers, which are nitrile dihydroboration intermediates.[9] When compared to the 1.5 kcal/mol preference determined for **1** over 2 equivalents of monomeric ($^{2,6\text{-}iPr2Ph}$BDI)MnH,[9] it becomes clear that bridging hydride ligands more effectively allow the Mn centres to enter a catalytic cycle. It is reasonable to propose that this relationship extends to coordination compounds throughout the transition series, and could be an important reason why hydride ligands are prevalent in homogeneous catalysis.

Conflicts of interest

The authors declare no competing financial interest.

Acknowledgements

Notes and references

‡ CCDC 2001029

1   P. P. Power, *Chem. Rev.*, 2012, **112**, 3482.
2   P. P. Power, *J. Organomet. Chem.*, 2004, ***689***, 3904.
3   P. L. Holland, *Acc. Chem. Res.*, 2008, **41**, 905.
4   C. Chen, S. M. Bellow and P. L. Holland, *Dalton Trans.*, 2015, **44**, 16654.
5   R. L. Webster, *Dalton Trans.*, 2017, **46**, 4483.
6   F. Basuli, H. Aneetha, J. C. Huffman and D. J. Mindiola, *J. Am. Chem. Soc.*, 2005, **127**, 17992.
7   J. Vela, J. M. Smith, Y. Yu, N. A. Ketterer, C. J. Flaschenriem, R. J. Lachicotte and P. L. Holland, *J. Am. Chem. Soc.*, 2005, **127**, 7857.
8   T. K. Mukhopadhyay, M. Flores, T. L. Groy and R. J. Trovitch, *Chem. Sci.*, 2018, **9**, 7673.
9   T. T. Nguyen, J.-H. Kim, S. Kim, C. Oh, M. Flores, T. L. Groy, M.-H. Baik and R. J. Trovitch, *Chem. Commun.*, 2020, **56**, 3959.
10 J. Chai, H. Zhu, H. Fan, H. W. Roesky and J. Magull, *Organometallics*, 2004, **23**, 1177.
11 J. Chai, H. Zhu, A. C. Stückl, H. W. Roesky, J. Magull, A. Bencini, A. Caneschi and D. Gatteschi, *J. Am. Chem. Soc.*, 2005, **127**, 9201.
12 S. Yao, Y. Xiong and M. Driess, *Chem. Eur. J.*, 2012, **18**, 11356.
13 M.-H. Baik, R. A. Friesner, G. Parkin, *Polyhedron*, 2004, **23**, 2879.
14 A. D. Bochevarov, E. Harder, T. F. Hughes, J. R. Greenwood, D. A. Braden, D. M. Philipp, D. Rinaldo, M. D. Halls, J. Zhang and R. A. Friesner, *Int. J. Quantum Chem.*, 2013, **113**, 2110.
15 A. D. Becke, *Phys. Rev. A Gen. Phys.*, 1988, **38**, 3098.
16 C. Lee, W. Yang and R. G. Parr, *Phys. Rev. B Condens. Matter*, 1988, **37**, 785.
17 S. Grimme, J. Antony, S. Ehrlich and H. Krieg, *J. Chem. Phys.*, 2010, **132**, 154104.
18 P. J. Hay and W. R. Wadt, *J. Chem. Phys.*, 1985, **82**, 270.
19 W. R. Wadt and P. J. Hay, *J. Chem. Phys.*, 1985, **82**, 284.
20 P. J. Hay and W. R. Wadt, *J. Chem. Phys.*, 1985, **82**, 299.
21 T. H. Dunning, *J. Chem. Phys.*, 1989, **90**, 1007.
22 G. te Velde, F. M. Bickelhaupt, E. J. Baerends, C. Fonseca Guerra, S. J. A. van Gisbergen, J. G. Snijders and T. Ziegler, *J. Comput. Chem.*, 2001, **22**, 931.
23 A. A. Rashin and B. Honig, *J. Phys. Chem.*, 1985, **89**, 5588.
24 L. Noodleman, *J. Chem. Phys.*, 1981, **74**, 5737.
25 B. D. Dunietz, M. D. Beachy, Y. Cao, D. A. Whittington, S. J. Lippard and R. A. Friesner, *J. Am. Chem. Soc.*, 2000, **122**, 2828.
26 G. A. Bain and J. F. Berry, *J. Chem. Educ.*, 2008, **85**, 532.
27 R. T. Azuah, L. R. Kneller, Y. Qiu, P. L. W. Tregenna-Piggott, C. M. Brown, J. R. D. Copley and R. M. Dimeo, *J. Res. Natl. Inst. Stand. Technol.*, 2009, **114**, 341.
28 S. Hansen and W. J. R. Müller-Warmuth, Pilbrow: Transition Ion Electron Paramagnetic Resonance, Clarendon Press, Oxford 1990. ISBN 0-19-855214-9. *Berichte der Bunsengesellschaft für physikalische Chemie*. 1991, pp 1307–1307.
29 R. D. Dowsing, J. F. Gibson, M. Goodgame and P. J. Hayward, *J. Chem. Soc. A*, 1969, **0**, 187.
30 R. D. Dowsing, J. F. Gibson, M. Goodgame and P. J. Hayward, *J. Chem. Soc. A*, 1970, **0**, 1133.
31 A. Bencini, D. Gatteschi, Electron Paramagnetic Resonance of Exchange Coupled Systems, Springer-Verlag: New York, 1990.
32 S. Stoll and A. Schweiger, *J. Magn. Reson.*, 2006, **178**, 42.
33 T. Nguyen, A. D. Sutton, M. Brynda, J. C. Fettinger, G. J. Long and P. P. Power, *Science*, 2005, **310**, 844.
34 L. Fohlmeister, S. Liu, C. Schulten, B. Moubaraki, A. Stasch, J. D. Cashion, K. S. Murray, L. Gagliardi and C. Jones, *Angew. Chem. Int. Ed.*, 2012, **51**, 8294.
35 I. Bernal, J. D. Korp, W. A. Herrmann and R. Serrano, *Chem. Ber.*, 1984, **117**, 434.
36 A. E. Ashley, R. T. Cooper, G. G. Wildgoose, J. C. Green and D. O'Hare, *J. Am. Chem. Soc.*, 2008, **130**, 15662.
37 W. Nolting and A. Ramakanth, *Quantum Theory of Magnetism*, Springer: Berlin, Heidelberg, 2009.
38 I. Dzyaloshinsky, *J. Phys. Chem. Solids*, 1958, **4**, 241.
39 J. Hicks, C. E. Hoyer, B. Moubaraki, G. Li Manni, E. Carter, D. M. Murphy, K. S. Murray, L. Gagliardi and C. Jones, *J. Am. Chem. Soc.*, 2014, **136**, 5283.
40 K. Fink, C. Wang and V. Staemmler, *Inorg. Chem.*, 1999, **38**, 3847.
41 B. Cordero, V. Gómez, A. E. Platero-Prats, M. Revés, J. Echeverría, E. Cremades, F. Barragán and S. Alvarez, *Dalton Trans.*, 2008, **21**, 2832.